Sensitivity to differential piston and to adaptive optics errors with the Large Binocular Telescope Interferometer

Patru, Fabien, Esposito, Simone, Puglisi, Alfio, Riccardi, Armando, Pinna, Enrico, et al.

SPIE.

Sensitivity to differential piston and to adaptive optics errors with the Large Binocular Telescope Interferometer

Fabien Patru[a], Simone Esposito[a], Alfio Puglisi[a], Armando Riccardi[a], Enrico Pinna[a], Carmelo Arcidiacono[a], John Hill[b], Philip Hinz[b]

[a] Osservatorio Astrofisico di Arcetri, 5 Largo Enrico Fermi, 50125, Firenze, Italia
[b] LBT Observatory, 933 N. Cherry Ave, AZ 85721, Tucson, United States

ABSTRACT

On-sky adaptive optics wavefront screens have been used and random optical path fluctuations - differential pistons - have been included in numerical simulations for the Large Binocular Telescope Interferometer. We characterize the Point Spread Function (PSF) and the Optical Transfer Function (OTF) by computing respectively the interferometric Strehl and the visibility criteria. We study the contribution of the wavefront disturbance induced by each adaptive optics system and by the optical path difference between the arms of the LBTI. To provide an image of quality (Strehl above 70%) suitable with standard science cases , the requirements for a LBTI mode in the visible wavelengths ($750nm$) must be at least an adaptive optics wavefront RMS fluctuations below $\lambda/18 \approx 40nm$ (Strehl above 90%) provided by each adaptive optics system, and a differential piston RMS fluctuations below $\lambda/8 \approx 100nm$ in the overall LBTI system. The adaptive optics wavefront errors - mainly the differential tip-tilt - appear to be more critical than the differential piston.

Keywords: Large Binocular Telescope Interferometer, interferometry, adaptive optics, point spread function, optical transfert function, wavefront aberrations, optical path difference, differential piston

1. INTRODUCTION

The LBTI (Large Binocular Telescope Interferometer) in Arizona can be used as an image-plane Fizeau interferometer, combining the beams from the two $8m$ primary mirrors of the LBT (Large Binocular Telescope) (1; 2). Preserving the phase information would allow true imaging over the field of view corrected by each single AO system. The first light adaptive optics (FLAO) have been used efficiently at the LBT by means of a pyramid wavefront sensor (3). First fringes were achieved in 2010, dual-aperture AO-corrected fringes in 2012 (4; 5), and first closed-loop observations with path length stabilization in 2013 (6). The LBTI can deliver the sensitivity of a $12m$ telescope and the spatial resolution of a $23m$ telescope, over a wide field of view of the order of few arcseconds square (7). We have shown (8) that the LBTI can also offer a significant gain in contrast, by properly combining the two separated wavefronts from each sub-aperture.

The study presented here has been initiated in the framework of the project LIVE (LBT Interferometer Visible Experiment) (9) proposed to the LBTO comity as a visible mode at the LBTI for exoplanets imaging. Providing phase screens reconstructed from FLAO on-sky data, a temporal sequence of frames is generated by a home-made simulation tool developed in INAF-Arcetri. Errors are introduced to reproduce realistic wavefronts corrected by a FLAO system and injected into the LBTI beam combiner. Those simulations provide results in agreement with numerical end-to-end simulations (8). Our study has been restrained to monochromatic light in the visible wavelengths ($\lambda = 750nm$). These results can be easily transposed into other wavelengths, since the specifications are expressed in unit of λ (*e.g.* RMS below a fraction of λ).

We review the numerous aberrations altering the LBTI performance (Sect. 2). Given an incoming wavefront with aberrations, we deduce the imaging properties by computing the Point Spread Function (PSF) and the Modulation Transfer Function (MTF) (Sect. 3). We study the contribution of the wavefront disturbance induced by each FLAO system and by the optical path difference (OPD) - or differential piston - between the arms of the LBTI (Sect. 4). We use FLAO data wavefronts for preliminary simulations to show the imaging capability of the LBTI (Sect. 4.1). We consider AO wavefronts with increasing root mean square (RMS) values, assuming perfect phased beams without residual piston (Sect. 4.2). We consider also differential pistons with increasing RMS values, assuming perfect AO wavefronts without any residual errors (Sect. 4.3). We study separately both effects which are assumed to be uncorrelated. We characterise the PSF and the MTF by computing respectively the interferometric Strehl and the visibility criteria. We explore as well other merit functions highlighting the LBTI behaviour (Sect. 5). We finally discuss on the requirements for the FLAO systems and on the needs for piston and tip-tilt sensing and correction systems (Sect. 6).

2. MAIN SOURCES OF ABERRATIONS

2.1 Overview of the aberrations in the LBTI

According to the LINC-NIRVANA error budget (10), the primary contributors reducing the LBTI performance are imperfect adaptive optics (AO) correction (across each sub-aperture) and uncorrected atmospheric piston (between both sub-apertures). We focus our study onto the effects of pistons and AO errors, assuming good seeing conditions and available bright reference stars. However, various effects - beyond the scope of this paper - can also alter the LBTI performance, like for instance:

- Differential piston errors (atmospheric, instrument, tracking, AO errors, etc.).
- Wavefront aberrations (atmospheric, telescope, instrument, AO errors etc.).
- Uncorrected spatial frequency beyond the AO cutoff frequency.
- Brightness amplitude mismatch (between the two channels of the LBTI).
- Surface quality of the optical components (surface roughness, figure errors, *vs* optical polishing procedure).
- Non-common path aberrations (between the sensing and the science channels).
- Vibrations (due to mechanical devices inside the interferometer).
- Misalignments, decentration losses (due to offsets between the de-rotation and the optical axis).
- Tracking errors, flexure inside the instrument (moving the PSF on the detector during an exposure).
- PSF decorrelation (occuring when the PSFs from the individual sub-aperture no longer overlap).
- Field rotation (rotational blurring of the PSF).
- Spectral bandwidth (chromatic blurring of the PSF, critical for a wide-band filter).
- Atmospheric dispersion (unavoidable chromatic effect, especially at low zenith angles).
- Polarization effects (induced by reflection from metallic mirrors).
- Pupil matching (differential shape of the pupil images).
- Distorsion.

2.2 Differential AO aberrations between the sub-apertures

AO performance is fundamentally limited by the seeing of the atmospheric turbulence and by the distribution and brightness of reference stars. The AO correction is optimum for the low order aberrations, decreases monotonically up to the AO cutoff frequency and is null for high order aberrations beyond the cutoff. The main errors contributions of a single AO system are due to the first orders. The tip-tilt is, by far, more significant than the contribution of the higher order aberrations (focus, astigmatism, etc.) (11).

The differential tip-tilt between the two AO-corrected sub-apertures can be seen as a jitter effect if both errors goes in the same direction, whereas it becomes critical if the tip-tilts goes in opposite direction. The same approach can be extrapolated to higher order aberrations, producing as well differential aberrations which compensate themselves or which adds in error contribution for each frame. The LBTI performance is firstly affected by the differential tip-tilts between the two AO-corrected sub-apertures.

2.3 Differential piston errors between the sub-apertures

Time-varying piston can arise from numerous effects (6; 12), such as the atmosphere, the AO system itself or the interferometer itself (neglected here). The atmosphere induces tip-tilts over the $23m$ baseline which translate into differential pistons between the two sub-apertures. The AO system provides flat wavefronts but cannot control the relative time of arrival of the wavefronts at the two telescopes. A piston bias can thus be introduced in normal operation, the piston being a degree of freedom for each AO system. The LBTI performance is secondly affected by the differential pistons which are either unseen or generated by both AO systems.

3. IMAGING PROPERTIES OF THE LBTI

3.1 LBTI aperture function

The aperture function reproduces the entrance pupil of the LBTI made of two primary mirrors of diameter $D = 8.4m$ having a central obscuration of diameter $0.9m$. Those mirrors have a center-to-center separation equal to the baseline $B = 14.4m$. The longest baseline, *i.e.* the maximum edge-to-edge separation of the LBTI aperture, reaches $B_{max} = B + D = 22.8m$. Assuming a uniform illumination of the entrance pupil - without scintillation -, the aperture function P equals to 1 within both sub-apertures and zero otherwise.

3.2 Complex amplitude of the incoming wavefront

The complex amplitude of the incoming wavefront is written as $P(\boldsymbol{r}) \cdot \exp[i\,\Phi(\boldsymbol{r})]$, which is a function of the aperture function (amplitude distribution) P and the aberrations function (phase distribution) of the wavefront expressed in meter W (differential pistons between two points in the pupil) or in radian $\Phi(\boldsymbol{r}) = 2\pi/\lambda\, W(\boldsymbol{r})$ (differential phase at a given wavelength). Aberrations are modelled by wavefront phase errors across each sub-apertures and piston errors between the two sub-apertures.

An aberrated wavefront across a sub-aperture is computed by means of phase screens reconstructed from FLAO on-sky data. Few temporal sequences of frames are generated by adjusting the phase RMS to reproduce realistic FLAO-corrected wavefronts in various conditions of turbulence. Those frames include all the residual AO aberrations: tip-tilt, focus and higher orders, as well as piston generated by each AO in normal operation, the difference of both absolute pistons being equal to the differential piston.

An atmospheric piston is added by applying a constant phase across one of the two sub-apertures. The piston fluctuations are generated in the sequence of frames by a random piston following a Gaussian distribution of zero-mean with a given RMS expressed as a fraction of wavelength. For each frame, two independent phase screens, with one of the two having a constant piston offset, are then included in the complex pupil function of the LBTI, before computing the imaging properties (PSF, MTF).

3.3 Point spread function (PSF)

The PSF equals to the square modulus of the Fourier transform of the complex amplitude at the entrance aperture of the LBTI: $PSF(\boldsymbol{x}) = |FT\{P(\boldsymbol{r}) \cdot \exp[i\,\Phi(\boldsymbol{r})]\}|^2$. The sampling of the PSF is set to 8 pixels per resolution element ($resel = \lambda/B_{max} = 6.785mas$ (milli-arc-second) for $\lambda = 750nm$). The image width is set to 512 pixels corresponding to a field of view of $64\,resels = 435mas$. The PSF is normalised here so that the maximum of the central fringe equals to 1 for a diffraction-limited exposure and equals to the Strehl ratio for a seeing-limited exposure.

The theoretical PSF is described by a fringe pattern within an Airy envelope (8). The aberrated PSF is disturbed by a scattered halo produced by wavefront aberrations in the complex amplitude. The short exposure PSF is computed from each individual frame of $\approx 1ms$. The long exposure PSF equals to the integration of 1000 frames (overall integration time of $\approx 1s$).
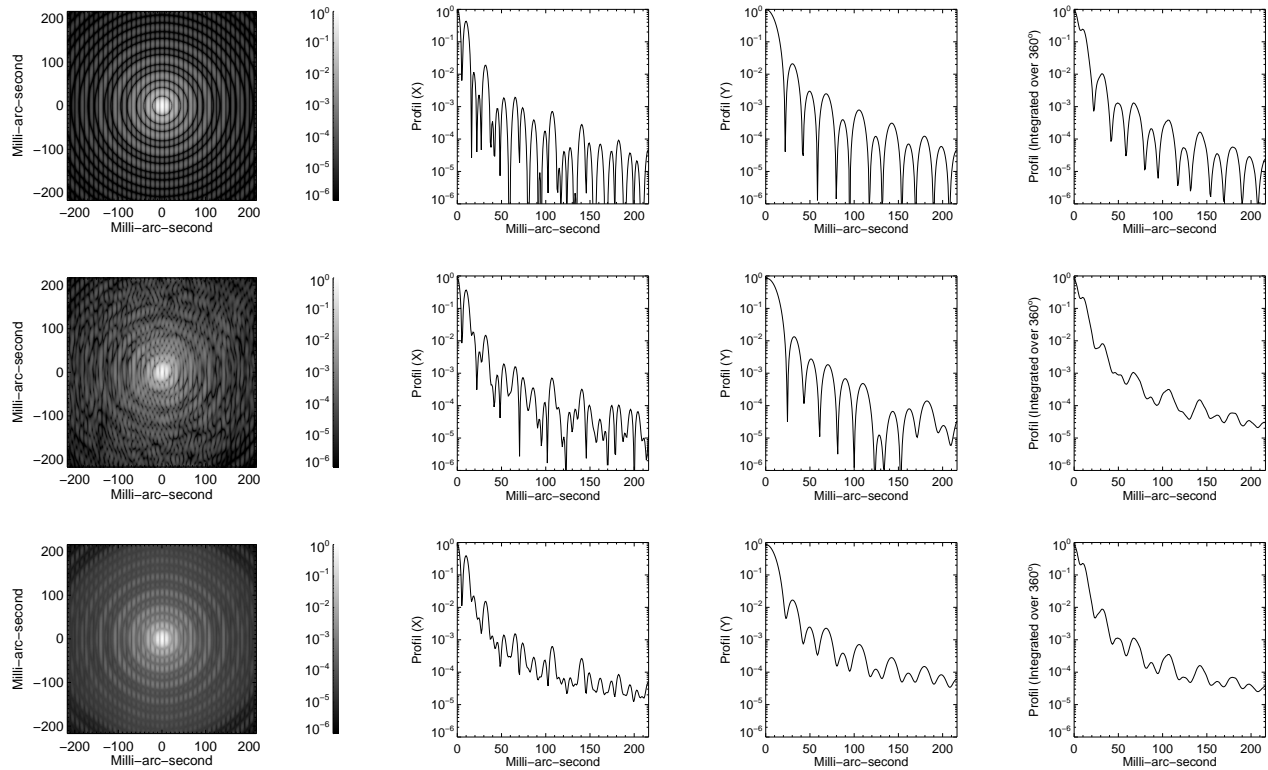
Figure 1. Theoretical PSF, short exposure PSF and long exposure PSF (top to bottom) of the LBTI in the visible wavelengths obtained by numerically combining two on-sky FLAO wavefronts having an AO Strehl of 90% in H band. Logarithmic distribution, X profile parallel to the baseline, Y profile perpendicular to the baseline, profile integrated over $360°$ (left to right). The LBTI can provide an interferometric Strehl above 85% in H band, assuming no differential errors in the optical train of the LBTI.

3.4 Modulation transfer function (MTF)

The Modulation Transfer Function (MTF) equals to the autocorrelation of the complex amplitude or to the modulus of the Fourier transform of the PSF: $MTF(\nu) = |FT\{PSF(\boldsymbol{x})\}|^2$. The MTF describes how the angular frequencies in the object space are transferred to the image space through the optical system. The sampling of the MTF is set to 4 pixels per frequency element of the MTF. The image width is set to 512 pixels, corresponding to the maximum angular frequency probed in the MTF equal to B_{max}/λ. The MTF is normalised so that the maximum of its central peak equals to 1 whatever the case.

The theoretical MTF is formed by a peak of width $2D/\lambda$ surrounded by two identical and weaker peaks of width D/λ at a distance B/λ from the axis. The central peak contains the low angular frequencies sampled by the short baselines within each $8.4m$ sub-aperture. The secondary peaks contain the high angular frequency information seen by the long baselines offered by both sub-apertures with baselines ranging from $14.4 - 8.4 = 6m$ to $14.4 + 8.4 = 22.8m$. The aberrated MTF is directly related to the image quality of the PSF. The long exposure MTF equals to the average of the short exposures MTF.

The small overlap of the high and low angular frequency peaks enables a complete frequency sampling (*i.e.* a full coverage of the UV plan) along the baseline axis, enabling image reconstruction by means of Earth rotation. However, angular frequency mixing occurs in this small overlap area. For example, the angular frequency at $7m/\lambda$ is mixed because it is sampled by both a single and two apertures at a time. A frequency sampled by a baseline spanning the two telescopes is biased by a differential piston, contrary to a frequency seen by a single aperture. The complex amplitudes add incoherently, resulting to a wrong piston value at this frequency.

4. LBTI RECOMBINATION OF TWO ON-SKY FLAO WAVEFRONTS

4.1 Numerical recombination of two FLAO wavefronts

As a benchmark, we use two data sets of FLAO wavefronts from on-sky observations (3) with an RMS of $\approx 100nm$ corresponding to an AO Strehl of 85% in H band (infrared) and 50% in R band (visible). The two data sets are separated in time by about two minutes, with the same atmospheric conditions (seeing, coherence time, wind speed, etc.) and the same AO parameters (magnitude of the guide star, number of corrected modes, gain, etc.). Each data set is used on each one of the two sub-apertures. The wavefront phase screens are reconstructed from the commands sent to the deformable mirror. However, it does not included the aliasing effect due to the sampling limit of the wavefront sensor, producing spurious low spatial frequency errors and edge-field halo in the PSF. Therefore, on-sky data are slightly biased, but only at the edge of the field of view provided by AO, which is beyond the field of view studied here.

The resulting PSFs of the LBTI at $\lambda = 750nm$ are shown in figure 1. We assume first no additional aberrations in the optical train of the LBTI combiner (*e.g.* neglected piston), apart from the differential errors between the two FLAO wavefronts. The aberrations of the FLAO wavefronts disturb the interferometric PSF of the LBTI in a similiar way as they disturb the single aperture PSF. Given a Strehl of 90% in H band for a single aperture, the interferometric Strehl (Sect. 5) of the LBTI reduces to $\approx 85\%$. This is an encouraging result showing that the image quality is preserved in the beam combiner. The interferometric Strehl which can be achieved by the LBTI equipped with two FLAO is close to the AO Strehl provided by a FLAO standalone, as long as other sources of aberrations can be mitigated. The imaging performance of the LBTI is thus fundamentally limited by the AO-correction level.

4.2 AO wavefronts with increasing RMS values

Short and long exposures of the PSFs of the LBTI at $\lambda = 750nm$ are shown in figures 2 and 4 with AO wavefront errors, assuming no piston. The wavefront amplitude of the FLAO dataset is adjusted to a certain RMS value, by multiplying each value of the wavefront by a constant value. We explore few RMS values ranging from $\lambda/64 \approx 10nm$ up to $\lambda/2 \approx 400nm$ in the visible wavelengths. The long exposure behaves in a similar way as the short exposures.

The tip-tilts induced by both AO systems onto each sub-aperture produce differential tip-tilts of the sub-beams and differential shifts of the sub-images, so that the diffraction envelopes do not overlap properly and the beams do not fully interfere coherently. The tip-tilt effects are negligible as long as the envelopes centres remain closely spaced with a separation less than a fraction of the envelope width λ/D. The tip-tilt effects are much more noticeable in the wings than near the center of the image, and thus reduce the usable field of view. The tip-tilt across a sub-aperture can be as much as about a radian, corresponding to 1/6 of a wavelength. Above 1 radian, tip-tilt becomes significant on the whole image. The overlap area of the diffraction envelopes - *i.e.* the coherent area containing the fringes - gets an ovoidal shape in the instantaneous PSF, while its circular shape is recovered by average in the long exposure PSF. For a tip-tilt larger than the width of the Airy envelope (*i.e.* RMS $> \lambda$), the differential tip-tilt is so high that the two beams no longer overlap, preventing fringe occurrence.

Short and long exposures of the MTFs of the LBTI at $\lambda = 750nm$ are shown in figures 2 and 5 with AO wavefront errors, assuming no piston. The long exposure behaves in a similar way than the short exposures. The AO wavefront aberrations (primarily the tip-tilt) disturb the shape of both the high and low angular frequency peaks. The MTF central peak of the LBTI dual-aperture is affected in the same manner as in the case of a single LBT aperture. Indeed, the MTF of the LBTI contains in its central peak the sum of the uncorrelated contribution from each one of the LBT aperture.

4.3 Differential pistons with increasing RMS values

Short and long exposures of the PSFs of the LBTI at $\lambda = 750nm$ are shown in figures 3 and 4 with piston errors, assuming no AO residual errors. The piston is adjusted to a certain RMS value, ranging from $\lambda/64 \approx 10nm$ up to $\lambda/2 \approx 400nm$ in the visible wavelengths. For large piston fluctuations, the fringes move back and forth within the Airy disk, reducing the fringe contrast for a long exposure, but not for a short one.
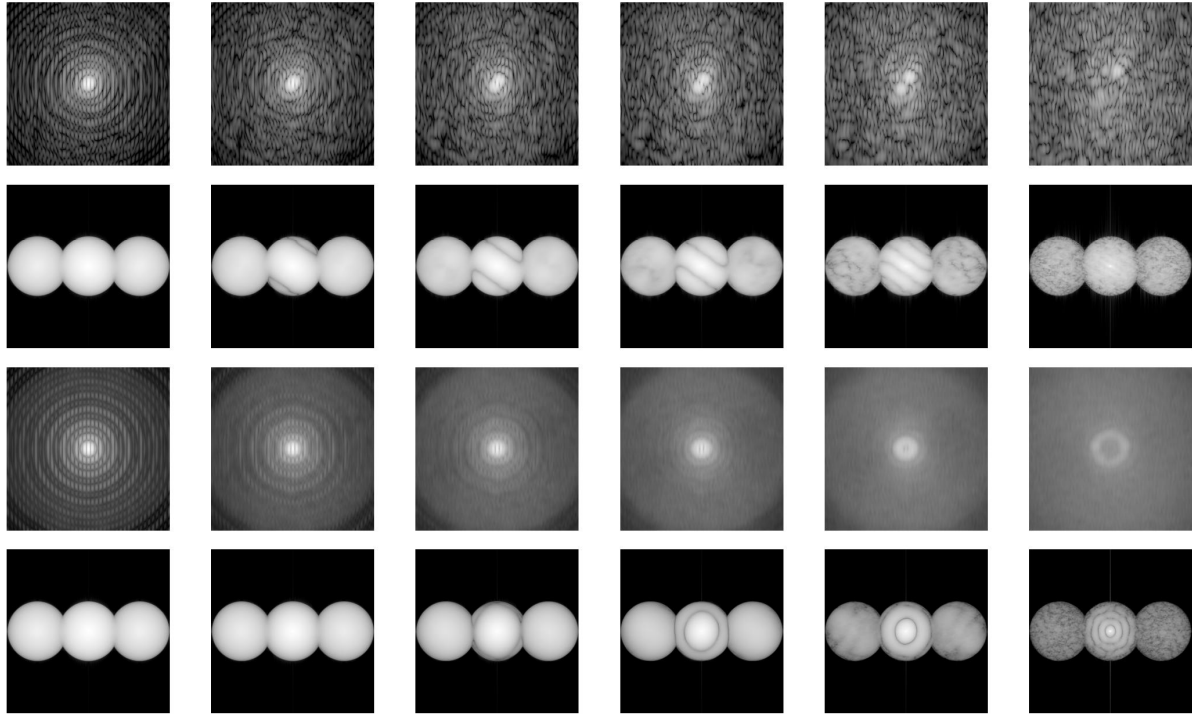
Figure 2. PSF and MTF distributions with AO wavefront errors, given an RMS equal to $\lambda/24, \lambda/12, \lambda/8, \lambda/6, \lambda/4, \lambda/2$ (left to right). Short exposure (top) and long exposure (bottom). Logarithmic scale. Same PSF spatial scale as in fig. 1.
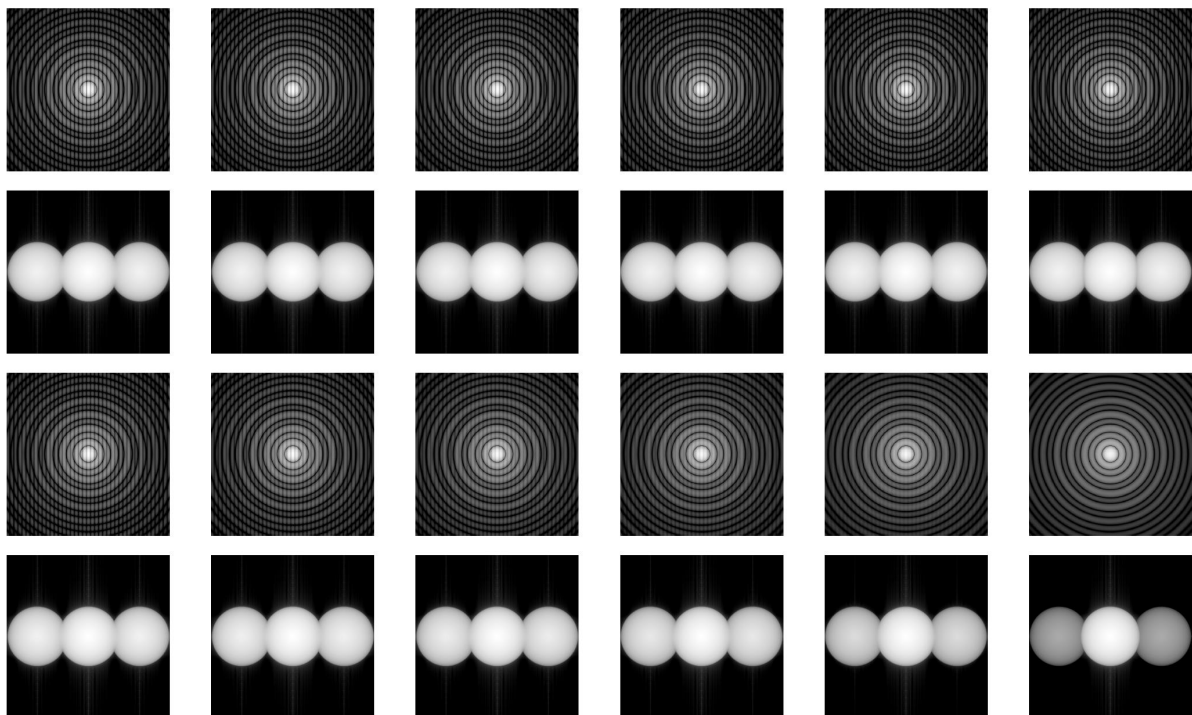

Figure 3. PSF and MTF distributions with piston errors. Same legend as in figure 2.
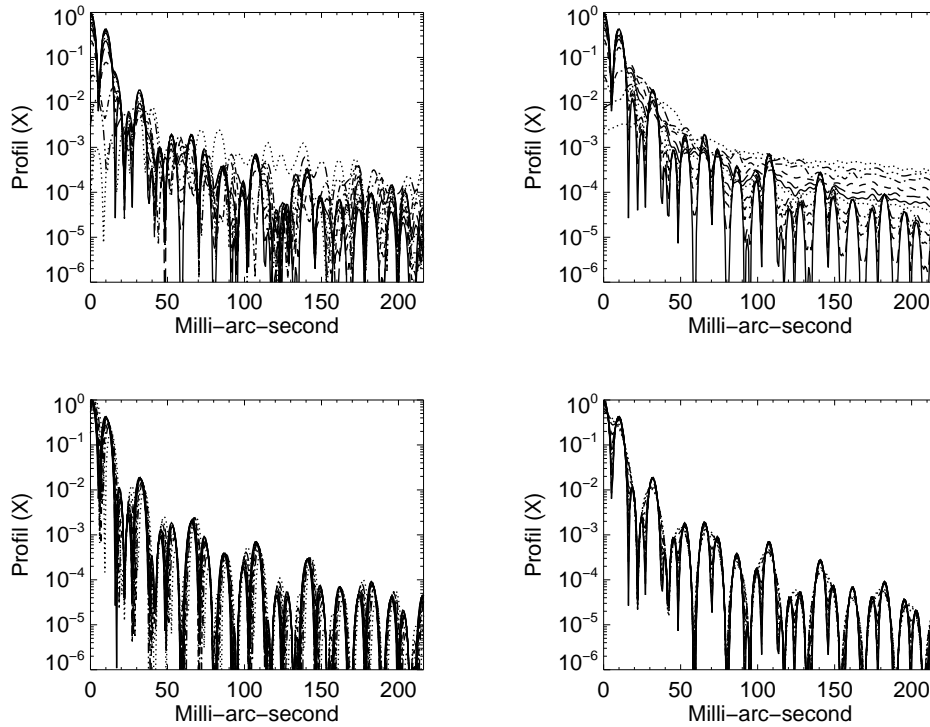
Figure 4. PSF profiles with AO wavefront errors (top) or with piston errors (bottom), given an RMS equal to 0 (solid line), $\lambda/64$ (long dash), $\lambda/32$ (dash), $\lambda/24$ (dash dot), $\lambda/18$ (dash dot dot), $\lambda/12$ (dot), $\lambda/10$ (solid line), $\lambda/8$ (long dash), $\lambda/6$ (dash), $\lambda/4$ (dash dot), $\lambda/3$ (dash dot dot), $\lambda/2$ (dot). Short exposure (left) and long exposure (right).
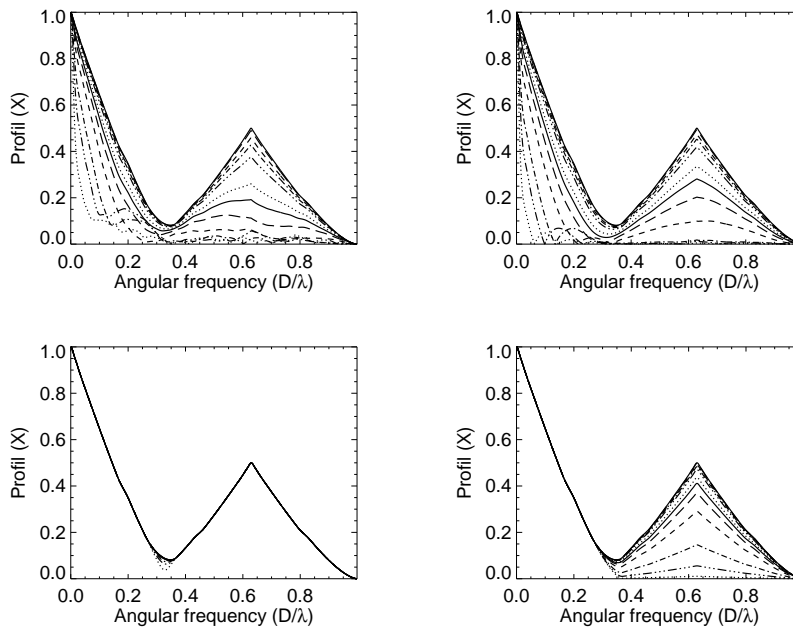

Figure 5. MTF profiles with AO wavefront errors (top) or with piston errors (bottom). Same legend as in figure 4.

For a short exposure, the piston varies over timescales much larger than the integration time of a single exposure (assuming a coherence time of the turbulence shorter than the exposure time), so that the fringe motion is frozen. The fringes are shifted by a random piston but their contrast remains unaffected. A snapshot exposure retains more high angular resolution information by freezing the fringes (8). A piston does not affect the fringe contrast in the instantaneous PSF, as long as the piston RMS remains below the coherence length $l_c = \lambda^2/2\Delta\lambda$, with $\Delta\lambda$ the spectral filter bandwidth.

For a long exposure, the piston varies over timescales much shorter than the whole integration time, producing a smearing of the fringes. The fringes are randomly shifted and blurred in the image. The final result is that the recorded fringes are no longer shifted, but their contrast is attenuated. The fringe contrast can be partially recovered by increasing the integration time, assuming stable conditions during the observation. Piston fluctuations affect the contrast in the long exposure PSF, which can be mitigated if the piston RMS remains below a fraction of wavelength.

Short and long exposures of the MTFs of the LBTI at $\lambda = 750nm$ are shown in figures 3 and 5 with piston errors, assuming no AO residual errors. The short exposure MTF is not disturbed by the piston errors (as for the PSF). Only the small area where the high and low angular frequency peaks overlap is slightly disturbed due to angular frequency mixing. In the long exposure MTF, the differential piston attenuates the amplitude of the high frequency peaks, whereas the low frequency peak remains unaffected. Indeed, the central peak is the sum of the contribution of both LBT apertures which have been assumed here perfectly corrected by AO.

5. MERIT FUNCTIONS

The LBTI performance can be described by a merit function accounting for the aberrations and for the image quality. We use and compare few criteria related to the features of the PSF and the MTF that change with aberrations. For the PSF (Fig. 6) : the interferometric Strehl, the contrast at a given radial distance. For the MTF (Fig. 7) : the visibility, the R23 quantity, the height and width of the central and secondary frequency peaks.

5.1 Interferometric Strehl of the PSF

The interferometric Strehl (10) - or "peak Strehl" (13) - is defined as the ratio of the maximum of the aberrated PSF to the maximum of the unaberrated PSF. The interferometric Strehl is insensitive to a fringes displacement induced by a residual piston and remains valid out-of-axis, contrary to the traditional Strehl ratio which is not suitable in the case of an interferometer (13). Thus, the interferometric Strehl accounts for the fact that the high angular frequency information delivered by the interferometer is retained in the short exposure PSF despite a shift of the fringes (Fig. 6). While the interferometric Strehl is almost insensitive to the piston errors for a short exposure, a loss of 15% corresponds to a residual piston RMS $\approx \lambda/8 \approx 100nm$ for a long exposure or to a residual AO wavefront RMS $\approx \lambda/18 \approx 40nm$ for both short and long exposures. The interferometric Strehl falls down below 50% for residual AO wavefronts RMS $> \lambda/8 \approx 100nm$ or for pistons RMS $> \lambda/2 \approx 400nm$.

5.2 Contrast of the PSF

We define the contrast of the PSF at a given radial distance r from the central axis integrated in all the directions (*i.e.* along a circle of radius r) and the averaged contrast of the PSF from r_1 to r_2 in all the directions (*i.e.* within a disk of radius r_2 having a central obscuration of radius r_1) . We consider the contrast from $80mas$ to $100mas$ (from 12 to 15 *resels*), as well as the contrast at $87mas$ (13 *resels*) and $95mas$ (14 *resels*). The contrast at $87mas$ and $95mas$ are located respectively at a local maximum and at a local minimum in the profile integrated over $360°$ (Fig. 1). For both short and long exposures, the contrast is insensitive to the piston errors, but is rapidly affected by AO errors.

The local minimum at $95mas$ corresponds to a dark ring - and a dark fringe -, yielding a valley between two side-lobes where the low irradiance enables locally a high contrast gain (8). A huge contrast is preserved for PSFs close to the diffraction limit, requiring AO errors better than $\lambda/64 \approx 12nm$ RMS for both short and long exposures (Fig. 6).
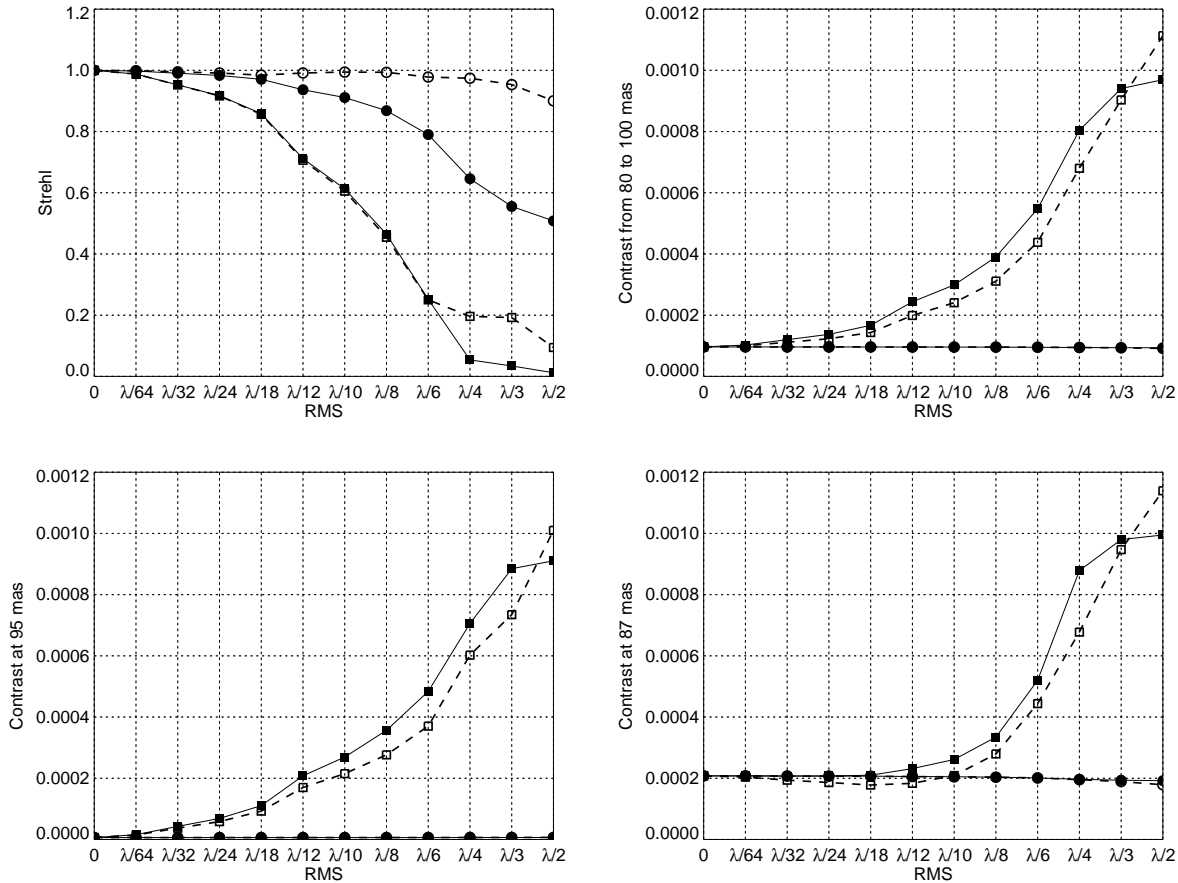
Figure 6. Merit functions for the PSF : Interferometric Strehl (top left), averaged contrast from $80mas$ to $100mas$ (top right), contrast at $95mas$ located in a local minima (bottom left), contrast at $87mas$ located in a local maxima (bottom right). AO wavefront errors (square symbol) or piston errors (circular symbol) for various RMS values. Short exposure (empty symbol, dashed line) and long exposure (filled symbol, solid line).

The local maximum at $87mas$ corresponds to a bright ring - and a bright fringe -, at the top of a side-lobe in the diffractive pattern where the high irradiance mitigates the achievable contrast (8). The contrast at the top of the side-lobe remains unaffected for AO errors below $\lambda/18 \approx 40nm$ for a long exposure, because the scattered halo firstly fills the valleys before altering the side-lobes.

The contrast gain in the valleys compared to the side-lobes is lost above $\lambda/12 \approx 60nm$ RMS. Indeed, the contrast reaches 2.10^{-4} at $\lambda/12$ RMS at $87mas$ and $95mas$, meaning that the valleys are fully filled by the scattered halo which completely smooths the diffractive pattern. The diffraction-limited PSF - made of fringes and Airy rings - reduces to a seeing-limited PSF - made of a central core surrounded by a speckle halo - (8).

5.3 Interferometric visibility of the MTF

The visibility (or fringes contrast) is defined as the square of the ratio of the integrated energy in the two secondary peaks of the MTF to the energy in the central frequency peak. However, the visibility is slightly biased by the overlap of the high and low angular frequency peaks. The visibility is defined here so that the overlapped energy is included only in the central peak, while the secondary peaks are slightly truncated, leading to a theoretical visibility of 0.985 instead of 1 (Fig. 7). Moreover, the visibility computation fails here for large AO errors (for RMS above $> \lambda/4$).
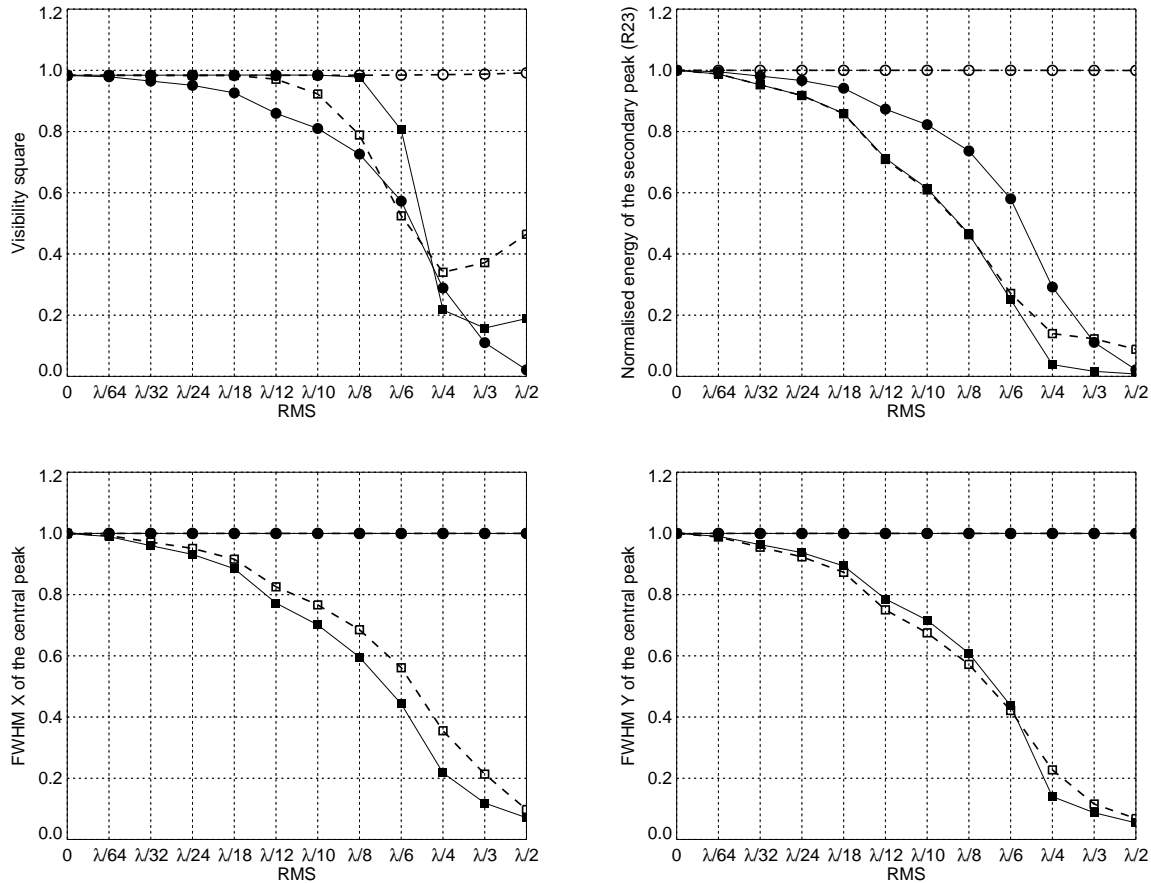
Figure 7. Merit functions for the MTF : Interferometric visibility (top left), R23 criteria (top right), FWHM X along the baseline (bottom left), FWHM Y perpendicular to the baseline (bottom right). Same legend as in figure 6.

While the visibility is insensitive to the piston errors for a short exposure, a loss of 15% corresponds to a residual piston RMS $\approx \lambda/12 \approx 60nm$ for a long exposure or to a residual AO wavefront RMS $\approx \lambda/6 \approx 130nm$ for both short and long exposures. The visibility falls down below 50% for residual AO wavefronts RMS $> \lambda/4 \approx 200nm$ or for pistons RMS $> \lambda/6 \approx 130nm$. For good AO correction, the visibility is almost not affected for both short and long exposures, because the energy of the high and low frequency peaks are reduced in the same proportion, so that the energy ratio remains unaffected. Indeed, as long as the two beams overlap, the fringes occur and the visibility is maximal. As soon as the beams no longer overlap sufficiently, the visibility drops down abruptly.

5.4 R23 quantity of the MTF

The quantity R23 is defined as the ratio of the integral of the high frequency peaks of the MTF to that under perfect conditions (14). R23 represents the fraction of the high angular resolution information that has been preserved in the images. Ideally, R23=1. While the R23 quantity is insensitive to the piston errors for a short exposure, a loss of 15% corresponds to a residual piston RMS $\approx \lambda/12 \approx 60nm$ for a long exposure or to a residual AO wavefront RMS $\approx \lambda/18 \approx 40nm$ for both short and long exposures (Fig. 7). The R23 quantity falls down below 50% for residual AO wavefronts RMS $> \lambda/8 \approx 100nm$ or for pistons RMS $> \lambda/6 \approx 130nm$.

Those results are in agreement with the results in the LINC-NIRVANA error budget (10) showing that R23 varies linearly for piston values below RMS $\approx \lambda/18 \approx 40nm$ (10). This is quite more optimistic than our requirement of RMS $\approx \lambda/12 \approx 60nm$. The specification for piston errors has been found below one tenth of the

observing wavelength in the infrared (RMS $< \lambda/10$ for R23>0.9) (10), while we would suggest a slightly higher specification in the visible wavelengths (RMS $> \lambda/15$ for R23>0.9).

5.5 Height and width of the peaks of the MTF

The width of a peak of the MTF is defined as to the full width at half maximum (FWHM), *i.e.* twice the radial distance from the centre of the peak where the height of the MTF is 0.5. The FWHM is normalised to the diffraction-limited value, leading to a value of 1 for the unaberrated FWHM. The FWHM X along the baseline and the FWHM Y perpendicular to the baseline behave similarly for both short and long exposures.

The peak widths are insensitive to differential piston errors. Indeed, assuming perfect flat wavefronts, the convolution of two top-hat functions equals to three frequency peaks of triangular shape, while piston errors only reduce the height of the secondary peaks. As expected, the height of the secondary peaks of the MTF (not shown here) behave similarly with the R23 quantity, those criteria characterising respectively the intensity and the energy of the peaks.

At the contrary, the widths of the secondary peaks (not shown here) increase and the width of the central peak decreases in the MTF as the AO wavefront errors increase (Fig. 7). The peak width narrowed by a factor of 15% corresponds to a residual AO wavefront RMS $\approx \lambda/18 \approx 40nm$. Then the width falls down below 50% for residual AO wavefront RMS $> \lambda/8 \approx 100nm$. For large AO errors, the FWHM X - respectively the FWHM Y - is slightly higher - respectively lower - in the short exposure than in the long exposure. While the central peak is centro-symmetric in a long exposure, fringes appear in a short exposure, yielding the differential FWHM in X and Y. Such fringes in the central peak are perpendicular to a shift of the two envelopes in the snapshot image (Fig. 2) and to the direction of the differential tip-tilt between the two beams in the entrance pupil. The fringes spacing reduces as the differential tip-tilt RMS increase. The amplitude and direction of the differential tip-tilt is therefore correlated to the fringes spacing and orientation in the central peak of the short exposure MTF.

6. DISCUSSION

6.1 Relevance of the merit functions

Few criteria have been evaluated as a merit function to characterise the PSF and the MTF quality. The interferometric Strehl and the R23 quantity appears as two relevant merit functions which behave similarly. The R23 quantity is even more sensitive to the contrast attenuation induced by the shift of the fringes in a long exposure (image blurring). The visibility should not be used as a merit function, but as a criterium for science applications. The contrast in the PSF enables to highlight two regimes depending on the location in the diffractive pattern, either in a side-lobe (low contrast) or in a valley (high contrast) (8).

The FWHM of the central and secondary peaks of the MTF may be used as additional criteria to sense the low order aberrations produced by each adaptive optics systems. For instance, large tip-tilt aberrations produces fringes in the central peak which can be sensed by comparing the FWHM in X and Y and which may be used to recover the differential tip-tilt induced by pointing errors of both telescopes.

6.2 Piston, tip-tilt effects

Piston errors induce, for a short exposure, a shift of the fringes within a fixed Airy envelope, preserving well-contrasted fringes. For a long exposure, piston errors induce a contrast loss of the fringes at a fixed position, due to image blurring. Tip-tilt errors induces, for both short and long exposures, a contrast loss of the fringes due to a shift of both Airy patterns which not overlap properly. Focus errors are less significant and behave similarly with both piston and tip-tilt effects (13). The effects of higher order aberrations produce mainly scattered light at the edge of the AO-corrected field, slightly reducing the maximum intensity while preserving the diffraction pattern at the center.

The effects of pistons and wavefronts aberrations are assumed here to be uncorrelated. However, both effects depend on the atmospheric conditions across a large turbulent cells of $23m$ of width feeding the two $8m$ telescopes, which can be correlated for instance by the atmospheric outer scale (of the order of few ten meters). Thus, the

simulations described here can be further improved by developing a end-to-end simulation tool. Post-treatment techniques may be applied on each individual frame, such as an adapted "shift-rotate-and-add" method or a more sophisticated deconvolution tool to enhance the image quality in each frame. A selection of high-quality frames may also be applied on the whole data set to improve the results.

6.3 Piston, tip-tilt tolerances and requirements

For a cophased regime, the piston tolerance is below the wavelength (piston $< \lambda/10$), *i.e.* the fringes displacement in the PSF has to be reduced to a fraction of ten of wavelength. The tip-tilt tolerance is lower than the angular resolution of a sub-aperture (tip-tilt $< \lambda/8.4m/10$), *i.e.* the position of each sub-image yielding the diffraction envelope in the PSF has to be stabilized to a fraction of ten of its width ($FWHM = \lambda/10D$). The performance of the LBTI depends critically on the performance of the AO systems (tip-tilt) and on the correction of the atmospheric piston. The requirements for a LBTI mode to provide an image of quality in the visible wavelengths ($750nm$) should be an AO wavefront RMS fluctuations below $\lambda/32 \approx 25nm$, or an AO Strehl above 90% in H band provided by each FLAO system, and a differential piston RMS fluctuations below $\lambda/8 \approx 100nm$ (for the interferometric Strehl) or $\lambda/12 \approx 60nm$ (for R23) in the overall LBTI system.

The AO wavefront errors - mainly the differential tip-tilt - appear to be more critical than the differential piston. The requirement to compensate the tip-tilt is higher than the requirement to cophase the beams in terms of RMS by a factor of the order of ≈ 3. If the differential tip-tilt effect dominates, a tip-tilt sensor and corrector on one or two arms of the LBTI would be required, in complement to a piston sensor and corrector.

6.4 Piston, tip-tilt sensing and correction at the LBTI

Piston and tip-tilt sensors are therefore needed to measure in real-time the tip-tilt fluctuations in the wavefronts from the two telescope beams and the piston fluctuations at the combined focus. A piston mirror moving back and forth is already used in the beam combiner to correct the piston in real-time. A tip-tilt mirror should be required as an upgrade for compensating the residual tip-tilt. A proper alignment of the LBTI should correct first the tip-tilts of the sub-apertures to overlap the sub-images before correcting the differential pistons.

Regarding the current on-sky performance of the LBTI in the infrared wavelengths, the two telescopes can ensure a pointing and tracking better than $\approx 0.3as$. The residual piston in closed-loop reaches currently $\approx 1\mu m$ RMS (6). An efficient piston and tip-tilt correction would be one of the main requirements for a visible mode, especially for nulling applications and/or if the FLAO performance goes down due to worse conditions of observation.

7. CONCLUSION

These results provide an estimate of the expected performance of the LBTI in the visible - and infrared - wavelengths, knowing the adaptive optics wavefronts RMS provided by the two FLAO systems and the residual piston RMS provided by the LBTI combiner against the atmospheric turbulence. An interferometric Strehl of 85% corresponds to a residual piston RMS $\approx \lambda/8 \approx 100nm$ or to a residual adaptive optics wavefront RMS $\approx \lambda/18 \approx 40nm$. An interferometric Strehl of $0.85^2 = 72\%$ corresponds to both effects at a time. In other words, an interferometric Strehl above 70% is achievable in the visible wavelengths, providing a piston below $100nm$ RMS and an AO correction better than $40nm$ RMS.

References

[1] Hill, J. M., Ashby, D. S., Brynnel, J. G., Christou, J. C., Little, J. K., Summers, D. M., Veillet, C., and Wagner, R. M., "The Large Binocular Telescope: binocular all the time," in [*Ground-based and Airborne Telescopes V*], *Proc. SPIE* **9145**, 914502 (July 2014).

[2] Hinz, P., Bailey, V. P., Defrère, D., Downey, E., Esposito, S., Hill, J., Hoffmann, W. F., Leisenring, J., Montoya, M., McMahon, T., Puglisi, A., Skemer, A., Skrutskie, M., Vaitheeswaran, V., and Vaz, A., "Commissioning the LBTI for use as a nulling interferometer and coherent imager," in [*Optical and Infrared Interferometry IV*], *Proc. SPIE* **9146**, 91460T (July 2014).

[3] Esposito, S., Riccardi, A., Fini, L., Puglisi, A. T., Pinna, E., Xompero, M., Briguglio, R., Quirós-Pacheco, F., Stefanini, P., Guerra, J. C., Busoni, L., Tozzi, A., Pieralli, F., Agapito, G., Brusa-Zappellini, G., Demers, R., Brynnel, J., Arcidiacono, C., and Salinari, P., "First light AO (FLAO) system for LBT: final integration, acceptance test in Europe, and preliminary on-sky commissioning results," in [*Proc. SPIE*], *Proc. SPIE* **7736**, 9 (July 2010).

[4] Hinz, P., Arbo, P., Bailey, V., Connors, T., Durney, O., Esposito, S., Hoffmann, W., Jones, T., Leisenring, J., Montoya, M., Nash, M., Nelson, M., McMahon, T., Pinna, E., Puglisi, A., Skemer, A., Skrutskie, M., and Vaitheeswaran, V., "First AO-corrected interferometry with LBTI: steps towards routine coherent imaging observations," in [*Optical and Infrared Interferometry III*], *Proc. SPIE* **8445**, 84450U (July 2012).

[5] Leisenring, J. M., Skrutskie, M. F., Hinz, P. M., Skemer, A., Bailey, V., Eisner, J., Garnavich, P., Hoffmann, W. F., Jones, T., Kenworthy, M., Kuzmenko, P., Meyer, M., Nelson, M., Rodigas, T. J., Wilson, J. C., and Vaitheeswaran, V., "On-sky operations and performance of LMIRcam at the Large Binocular Telescope," in [*Ground-based and Airborne Instrumentation for Astronomy IV*], *Proc. SPIE* **8446**, 84464F (Sept. 2012).

[6] Defrère, D., Hinz, P., Downey, E., Ashby, D., Bailey, V., Brusa, G., Christou, J., Danchi, W. C., Grenz, P., Hill, J. M., Hoffmann, W. F., Leisenring, J., Lozi, J., McMahon, T., Mennesson, B., Millan-Gabet, R., Montoya, M., Powell, K., Skemer, A., Vaitheeswaran, V., Vaz, A., and Veillet, C., "Co-phasing the Large Binocular Telescope: status and performance of LBTI/PHASECam," in [*Optical and Infrared Interferometry IV*], *Proc. SPIE* **9146**, 914609 (July 2014).

[7] Herbst, T. M., Ragazzoni, R., Eckart, A., and Weigelt, G., "LINC-NIRVANA: the Fizeau interferometer for the Large Binocular Telescope," in [*Optical and Infrared Interferometry*], *Proc. SPIE* **7013**, 701326 (July 2008).

[8] Patru, F., Puglisi, A., Riccardi, A., Pinna, E., Arcidiacono, C., Hill, J., and Hinz, P., "Fundamental gain in high contrast imaging with the Large Binocular Telescope Interferometer," in [*This proceeding*], *Proc. SPIE* (2016).

[9] Hinz, P., Esposito, S., Apai, D., Brusa, G., Close, L., Guyon, O., Hill, J., Males, J., Pinna, E., and Puglisi, A., "Toward visible wavelength coherent imaging with the LBT," in [*Optical and Infrared Interferometry IV*], *Proc. SPIE* **9146**, 914605 (July 2014).

[10] Herbst, T. M., Ragazzoni, R., Eckart, A., and Kurster, M., "LINC-NIRVANA Error Budget, Doc. No. LN-MPIA-FDR-GEN-001," (2005).

[11] Noll, R. J., "Zernike polynomials and atmospheric turbulence," *Journal of the Optical Society of America (1917-1983)* **66**, 207–211 (1976).

[12] Bailey, V. P., Hinz, P. M., Puglisi, A. T., Esposito, S., Vaitheeswaran, V., Skemer, A. J., Defrère, D., Vaz, A., and Leisenring, J. M., "Large binocular telescope interferometer adaptive optics: on-sky performance and lessons learned," in [*Adaptive Optics Systems IV*], *Proc. SPIE* **9148**, 914803 (July 2014).

[13] McCarthy, D. W., Sabatke, E. M., Sarlot, R. J., Hinz, P. M., and Burge, J. H., "Cryogenic beam-combiner for very low background 2- to 20-um interferometry on the 22.8-m Large Binocular Telescope," in [*Interferometry in Optical Astronomy*], Léna, P. and Quirrenbach, A., eds., *Proc. SPIE* **4006**, 659–672 (July 2000).

[14] Egner, S. E., Herbst, T. M., and Arcidiacono, C., "General performance analysis of a Fizeau interferometer," in [*Optical and Infrared Interferometry*], *Proc. SPIE* **7013**, 70133C (July 2008).